Coherent control of solid-state defect spins via patterned boron-doped diamond circuit

Masahiro Ohkuma[1,*] Eikichi Kimura[1,*] Eunsang Lee[2,*] Ryo Matsumoto[3,†] Shumpei Ohyama[1], Saki Tsuchiya[1], Harim Lim[2], Yong Soo Lee[2], Yoshihiko Takano[3], Junghyun Lee[2,4,‡] and Keigo Arai[1§]

[1]*School of Engineering, Institute of Science Tokyo, Yokohama, Kanagawa 226-8501, Japan*
[2]*Center for Quantum Technology, Korea Institute of Science and Technology, Seoul, 02792, Republic of Korea*
[3]*Research Center for Materials Nanoarchitectonics (MANA), National Institute for Materials Science, Tsukuba, Ibaraki 305-0047, Japan and*
[4]*Department of Quantum Information, Korea National University of Science and Technology (UST), Seoul 02792, Republic of Korea*

We demonstrate the coherent control of nitrogen-vacancy (NV) spins using an electronic circuit integrated within diamond: a patterned, conductive boron-doped diamond (BDD) microwave waveguide. First, we validate the high-frequency performance of the circuit by characterizing its impedance up to the microwave range, confirming microwave transmission sufficient for optically detected magnetic resonance (ODMR) and coherent Rabi control. Under ambient conditions, we perform ODMR and observe Rabi oscillations driven by the heavily-doped BDD circuit. We verify that microwave-induced frequency shifts remain limited under the present operating conditions at room temperature. In addition, separate high-pressure and low-temperature continuous-wave ODMR measurements demonstrate that the BDD antenna remains operational as a microwave delivery element in a high-pressure and low-temperature environment. These results indicate the potential of BDD circuits for on-chip microwave delivery in NV-based quantum devices, particularly for ODMR operation under extreme conditions.

Diamond is a versatile material capable of accommodating various impurities that substantially alter its electronic, thermal, and optical properties. Among these, boron doping is a well-known technique for transforming diamond into a p-type semiconductor. With sufficient doping, diamond can exhibit metallic behavior and superconductivity at cryogenic temperatures [1–4]. Boron-doped diamond (BDD) can be grown into thin films via microwave plasma chemical vapor deposition, enabling the development of advanced devices, such as superconducting quantum interference devices and microwave components [5–8]. These BDD thin films support the transmission of alternating electric currents across a broad frequency range, thereby showing great potential for use in electric circuits. With such unique electrical and physical properties, BDD holds great promise for cutting-edge applications in both power electronics [9–11] and quantum technologies [12].

The negatively charged nitrogen-vacancy (NV) center—a point defect in the diamond lattice—has become a leading platform for quantum measurement, owing to its unique properties [13–22]. One of its most striking features is the ability to maintain coherent spin control under extreme conditions: from ultrahigh vacuum to pressures as high as 130 GPa [23–25] and temperatures ranging from cryogenic to a blazing 1400 K [26–29]. This capability enables NV-based magnetometry to become a powerful platform for exploring physical phenomena under extreme conditions [24, 25, 30–33]. These applications rely on the use of alternating electromagnetic fields across a broad frequency spectrum: gigahertz microwaves for manipulating electronic spin ground states [34], megahertz radio frequencies for nuclear spin control [35–37], and kilohertz currents for modulating electronic spin states [38, 39]. These fields are generated using metal-based circuits made from materials such as gold or copper, often layered atop a thin titanium adhesive film. However, metal-based microwave structures can present practical limitations in certain environments, motivating the exploration of alternative materials. Therefore, conductive BDD provides an alternative material platform for microwave circuits where mechanical and chemical robustness are required.

In this letter, we demonstrate a diamond-compatible integrated architecture in which an Ω-shaped BDD thin film circuit serves as a broadband source of alternating magnetic fields for coherent control of an ensemble of NV centers in diamond. Our key findings are as follows: (i) the impedance of the BDD thin films was accurately modeled by a lumped parameter circuit model up to 3 GHz; (ii) BDD with high boron concentration generated microwave fields with sufficient intensity to drive Rabi oscillations, and (iii) microwave-induced frequency shifts remain limited under the present operating conditions at room temperature. In addition, to demonstrate the applicability of the BDD antenna under extreme conditions, we performed ODMR measurements using the BDD antenna under high-pressure and low-temperature conditions below 20 K. These results demonstrate coherent NV-spin control under ambient conditions and microwave delivery under high-pressure and low-temperature conditions. In the following sections, we provide details of our experimental results and discuss the implications of this

* These authors contributed equally to this work.
† MATSUMOTO.Ryo@nims.go.jp
‡ jh_lee@kist.re.kr
§ arai.k.835f@m.isct.ac.jp

technology.

The BDD–NV hybrid system comprises an Ω-shaped BDD circuit grown by masked microwave plasma chemical vapor deposition on a diamond hosting a 4.5 ppm ensemble of NV centers, as illustrated in Fig. 1. After hot mixed acid treatment of the diamond surface, the circuit pattern was prepared by electron-beam lithography and a Ti/Au metal mask was formed by lift-off. The masked substrate was annealed under vacuum to form a TiC adhesion layer at the Ti/diamond interface, followed by BDD growth using methane and trimethylboron as the carbon and boron sources. The metal mask was then removed by hot mixed acid treatment. By repeating this process with different trimethylboron-to-methane flow-rate ratios, three Ω-shaped BDD circuits with different boron concentrations were fabricated on the same NV-diamond substrate. The boron concentrations are determined via an analysis of the temperature dependence of resistivity, as presented in Table I [2, 40]. The microwave signal was delivered to the BDD circuits through a 50 Ω printed circuit board and a 25-μm-diameter Au wire attached with Ag paste. Further details are provided in the Supplementary Material. Impedance measurements further indicate that the BDD circuit can deliver microwaves to the NV centers. Although the circuit was not optimized for 50 Ω, it generated a microwave magnetic field sufficient to drive MHz-scale Rabi oscillations of the NV ensemble. Details of the electrical resistivity and impedance measurements are provided in the Supplemental Material. For the high-pressure experiments, a separate diamond anvil was also patterned with a BDD circuit using the same masked growth process, as shown in the inset of Fig. 4(b). This BDD-patterned diamond anvil was used as the microwave delivery element in the diamond anvil cell.

The NV center possesses an electronic ground-state triplet characterized by the states $|0\rangle$ and $|\pm1\rangle$, with a separation of 2.87 GHz resulting from spin–spin interactions. Additionally, the $|\pm1\rangle$ states experience further splitting due to the Zeeman effect when subjected to a finite magnetic field B aligned with the NV axis of interest. The energy levels corresponding to these spin states can be analyzed via optically detected magnetic resonance (ODMR) spectroscopy, which involves observing changes in the red fluorescence of the NV center as the microwave field frequency matches the energy difference between the $|0\rangle$ state and either of the $|\pm1\rangle$ states [41, 42]. The electrical conductivity of the BDD circuit was confirmed by dc transport measurements, while its high-frequency response and microwave-delivery capability were evaluated by impedance measurements and coherent NV spin-control experiments. Experimental details are described in Supplemental Material.

First, continuous-wave (CW) ODMR and Rabi oscillation measurements between the $|0\rangle$ and $|-1\rangle$ states are performed using BDD-based Ω-shaped circuits under a static magnetic field of 4.5 mT. Figs. 2a and b show data collected near the centers of three BDD structures. The measured ODMR contrasts and FWHMs at ∼2.7 GHz are $(0.8 \pm 0.2)\%$ and 4 ± 1 MHz (BDD1), $(0.9 \pm 0.1)\%$ and 4 ± 1 MHz (BDD2), and $(0.20 \pm 0.09)\%$ and 2 ± 1 MHz (BDD3), respectively. Rabi frequencies were 6.62 ± 0.04 MHz for BDD1 and 4.19 ± 0.06 MHz for BDD2 at a microwave input power of 46.5 dBm, consistent with the impedance data indicating enhanced mi-

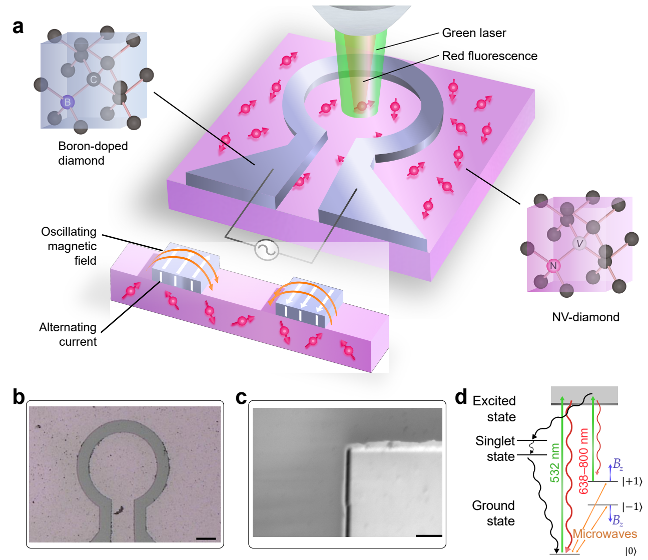

FIG. 1. (a) (Top) Overview of BDD–NV system comprising a Ω-shaped BDD circuit fabricated on a diamond substrate containing an ensemble of NV centers. In this study, we measured NV centers mainly inside the Ω area. Crystal structure of BDD is shown in the left side. Structure of NV center in diamond lattice is shown in the right side. N and V denote nitrogen atom and vacancy, respectively. (Bottom) Side view of BDD–NV system. A BDD thin film is grown on a single-crystalline diamond containing NV centers. The Ω-shaped BDD circuit hosts an alternating current at the microwave frequency range, generating an oscillating magnetic field. This microwave field is used for manipulating the NV centers in the diamond substrate. (b) Optical micrograph of BDD circuit with boron concentration of 3×10^{21} cm^{-3}. Scale bar is 50 μm. (c) Scanning electron microscope image of an edge of BDD thin film grown on single-crystalline diamond substrate with NV centers. Scale bar is 10 μm. (d) Energy diagram of NV center. The ground states can be excited optically by a 532 nm laser and decay along with spin-dependent fluorescence. The spin state is manipulated by a microwave magnetic field applied by a BDD circuit.

TABLE I. Parameters of BDD circuits. ρ and R. T. denote resistivity and room temperature, respectively. Boron concentration is estimated based on the temperature dependence of resistivity.

	BDD1	BDD2	BDD3
ρ (Ω cm) at R. T.	9.8×10^{-4}	4.1×10^{-3}	5.8×10^{-1}
B concentration (cm^{-3})	3×10^{21}	4×10^{20}	1×10^{20}
Thickness (nm)	780	640	690

crowave delivery in lower-resistivity samples. No Rabi oscillation is observed in BDD3 owing to its high resistivity. The definitions and estimation procedures for the CW ODMR and Rabi contrasts are described in the Supplementary Material. Although both the CW ODMR and Rabi contrasts are modest under the present conditions, they are likely dominated by non-optimized optical initialization and readout conditions rather than insufficient microwave delivery. Moreover, Rabi oscillations in BDD1 were measured at input powers of 646, 1310, and 1683 mW, as shown in Fig. 2c. The corresponding Rabi frequencies are 6.83, 9.48, and 10.6 MHz, respectively. These data are plotted in Fig. 2d, which shows the expected linear relationship between the square root of the applied microwave power and Rabi frequency. Rabi oscillations were observed throughout the Ω-shaped BDD1 region, as shown in the Supplementary Material. In the central approximately 50 μm × 50 μm region, the measured Rabi frequency showed a median value of 7.81 MHz with a standard deviation of 0.49 MHz, corresponding to a relative standard deviation of approximately 6%.

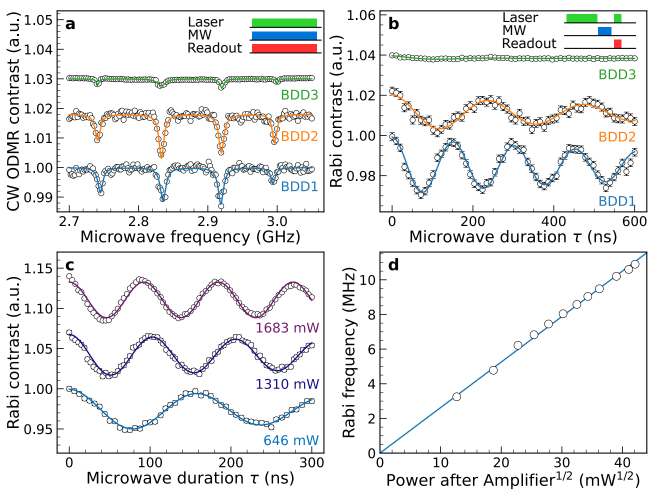

FIG. 2. (a) ODMR spectra measurement result using different BDDs with varied boron densities. The spectra are offset by 0.015 for BDD2 and 0.03 for BDD3. (b) Rabi oscillations using different BDD circuits and the pulse sequence used for Rabi measurement (inset). Rabi contrasts are offset by 0.02 for BDD2 and 0.04 for BDD3. These signals are obtained at the center of each Ω-shaped circuit. Each spectrum is normalized by its respective maximum intensity. (c) Rabi oscillations measured in BDD1 antenna at different input powers: 646, 1310, and 1683 mW. The data are vertically offset by 0.07 for 1310 mW and 0.14 for 1683 mW for clarity. The corresponding Rabi frequencies at each input power were 6.83, 9.48, and 10.6 MHz, respectively. (d) Input microwave power dependence of Rabi oscillation frequency. The result shows $\Omega \propto \sqrt{P_{\mathrm{MW}}}$.

To assess the thermal effects of the BDD microwave antenna during NV spin control, we performed two measurements: long-duration Rabi chevron mapping and off-resonant microwave driving followed by Ramsey interferometry. Previous studies have shown that temperature variations in the sample predominantly shift the zero-field splitting (ZFS) of the NV center, affecting the spin-state transition resonance frequencies [43]. Heating-induced frequency shifts from metallic microwave antennas have been previously reported [44].

To probe potential resonance shifts during rapid driving, we performed a full Rabi chevron measurement (Fig. 3a), sweeping the microwave frequency from −25 to +25 MHz around the resonance at 2.7405 GHz and the microwave signal duration up to 1 μs in 10 ns steps. The resulting chevron does not show the asymmetry expected for a large thermally induced resonance shift, as illustrated by the simulation in the Supplemental Material. The symmetric chevron pattern indicates that any thermally induced resonance shift during the short-duration Rabi experiment is not large enough to noticeably distort the observed pattern under the present conditions.

Ramsey spectroscopy between the $|0\rangle$ and $|-1\rangle$ states was employed to quantify temperature-induced shifts resulting from off-resonant microwave driving with varied power and duration. To resolve hyperfine-split Ramsey fringes, the $\pi/2$ pulses were detuned by +3 MHz from the NV resonance, while a 400 MHz-detuned microwave pulse was applied to induce heating. Frequency shifts in the Ramsey signal were recorded as a function of microwave power and pulse duration. The total microwave energy $E = P \times t$ was varied by tuning both power (via expected Rabi frequency) and duration, and the resulting Ramsey frequency shifts were extracted using a fast Fourier transform (FFT) analysis (See Supplemental Information for the more details). As the total input energy increased, the Ramsey FFT peak shifted to higher frequencies, capturing the negative shift in ZFS with temperature rise (Fig. 3b). Notably, the maximum frequency shift observed for a 10 μs microwave pulse duration with an 11 MHz Rabi frequency is approximately 1 MHz, which corresponds to an estimated temperature rise of approximately 14 K.

In the sequences considered here, we employed a Rabi frequency on the order of 10 MHz, which results in a spectral bandwidth of the same order. Consequently, the thermally induced shift represents only ∼ 10% of the excitation bandwidth, ensuring that the NV centers remain effectively driven within the spectral width of the control pulse. Furthermore, the observed frequency shift (∼1 MHz) is smaller than the hyperfine splitting induced by NV host nuclear spins, such as 2.16 MHz (^{14}N) or 3.03 MHz (^{15}N) [45]. The frequency shift remains below the hyperfine separation, so it does not qualitatively increase cross-talk to adjacent hyperfine transitions. Thus, under the present operating conditions, the measured frequency shift is limited compared with the excitation bandwidth used for coherent spin control. On the other hand, the observed shift indicates measurable microwave-induced heating under long off-resonant microwave exposure.

To assess the operational robustness of the BDD antenna under extreme conditions, we performed ODMR

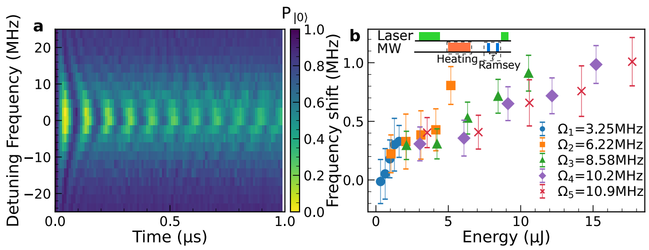

FIG. 3. (a) Rabi chevron measurement result using BDD1 antenna. Rabi oscillations are measured by sweeping the microwave frequency from -25 to $+25$ MHz and the microwave signal duration up to 1 μs in 10 ns steps. $P_{|0\rangle}$ represents the probability of preserving the initial state $|0\rangle$. (b) Plot of frequency shift as a function of the total applied energy, along with the pulse sequence used for the measurement (inset). To quantify the heating effect, the $\pi/2$ pulses in the Ramsey sequence are detuned by $+3$ MHz from the NV resonance frequency (blue box in the inset), and an additional microwave pulse detuned by 400 MHz was applied before the Ramsey sequence (orange box in the inset). The total energy, shown on the horizontal axis, is calculated as $E = P \times t$, where P is the applied microwave power, and t is the pulse duration (i.e., the width of the orange box). The legends indicate the Rabi frequencies corresponding to each input power. A longer heating time results in a larger frequency shift.

measurements in a diamond anvil cell using a BDD-patterned diamond anvil. This high-pressure device is distinct from the BDD–NV hybrid substrate used in the ambient-pressure measurements described above. In the high-pressure experiment, the BDD circuit was fabricated on a diamond anvil and used as the microwave delivery element, while a microdiamond with NV centers was placed in the sample chamber, as described in the Supplemental Material. To reduce possible systematic effects associated with microwave-induced heating, the ODMR spectra were acquired using alternating MW-off and MW-on measurements, as illustrated in the inset of Fig. 4a.

Figure 4a shows ODMR spectra measured below 20 K. The pressure was changed in situ during the experiment. We label the measurement points as P0–P9.

Starting from ambient pressure (P0), the pressure was first increased to the highest-compression state (P1), and then the sample chamber was gradually decompressed back toward ambient pressure while ODMR spectra were recorded at P2–P9. ODMR signals were observed at all measurement points from P0 to P9, demonstrating that the BDD-patterned diamond anvil remained functional as a microwave delivery element throughout both compression and decompression. The relatively low ODMR contrast at P0 is attributed to the lower microwave input power than that in P1–P9.

The evolution of the ZFS shift during compression and decompression is shown in Fig. 4b. The maximum ZFS shift observed in this experiment was approximately 220 MHz, which would correspond to approximately 15 GPa if the pressure coefficient of 14.58 MHz/GPa is assumed [46]. Importantly, ODMR signals were still observed after decompression, indicating that the same BDD-patterned anvil maintained electrical continuity after pressure loading and pressure release and could be reused after cleaning. Thin metal films placed near the surface of the diamond anvil can suffer from deformation or breakage after pressure loading [47]. This result supports the mechanical robustness of the patterned BDD structure itself and highlights its potential as a diamond-compatible microwave delivery element compared with conventional metal thin-film structures.

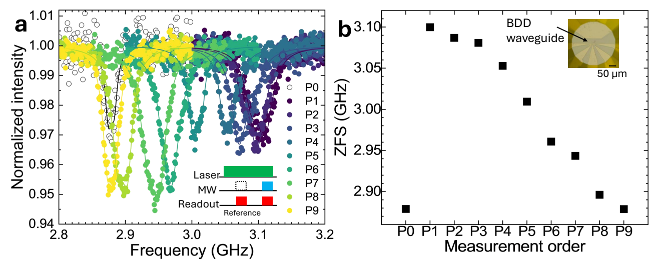

FIG. 4. High-pressure and low-temperature ODMR measurements using a BDD-patterned diamond anvil. (a) CW ODMR spectra of a microdiamond with NV centers measured below 20 K in a diamond anvil cell. The measurement points are labeled P0–P9. Starting from ambient pressure (P0), the pressure was increased to the maximum pressure (P1) and then gradually released while ODMR spectra were recorded at P2–P9. The inset schematically shows the alternating MW-off and MW-on measurement scheme used to acquire the ODMR spectra. (b) Evolution of the ZFS shift during compression and decompression. ODMR signals were observed throughout both compression and decompression, indicating that the BDD-patterned diamond anvil remained functional as a microwave delivery element under high-pressure and low-temperature conditions. The inset shows an optical image of the BDD-patterned diamond anvil used in the high-pressure ODMR measurements.

In this letter, we show that coherent control of NV centers can be achieved using a BDD-based circuit under ambient conditions. Together with the high-pressure CW ODMR measurements using a BDD-patterned diamond anvil, these results demonstrate the potential of BDD circuits as diamond-compatible microwave delivery elements for NV-based quantum sensing under extreme conditions. The impedance behavior observed in our system is well described by a parallel R–C circuit model (See Supplemental Information for the more details), offering a solid foundation for future improvements. One direct route to enhance circuit efficiency is minimizing the resistivity of the BDD material. Previous studies have shown that boron concentration can reach up to 1×10^{22} cm^{-3} [48], pushing the Hall carrier concentration to similar levels. However, even with such ultra-high doping, the reduction in resistivity is expected to be limited to a factor of approximately three compared to the current devices. Therefore, to achieve substantial performance gains, it is essential to combine high doping with structural optimizations. Strategies such as increasing the BDD film thickness to reduce sheet resistance, or tuning the dimensions of the current Ω-shaped loop, will be crucial. Moreover, the applicability of BDD is not limited to the simple loop design used in this study. In the field of NV-based quantum sensing, various antenna architectures have been developed such as coplanar waveguides and split-ring resonators [49, 50]. Since our BDD fabrication process is compatible with standard lithography, these advanced geometries can be readily implemented using BDD. Adopting such designs would allow the performance of the BDD–NV hybrid system to be further tailored to specific application needs, such as wider bandwidths or lower power consumption.

Employing BDD circuits for microwave delivery offers several key advantages, particularly their exceptional physical and chemical robustness, as well as their compatibility with integrated device architectures. BDD is chemically stable across a wide pH range, rendering it ideal for use in both acidic and alkaline environments; an asset that has already proven valuable in electrochemical applications [51, 52]. Moreover, it can withstand extreme conditions, including high temperatures and pressures, and remains reusable after returning to ambient conditions [40, 53, 54]. Furthermore, BDD circuits can be precisely microfabricated. By introducing insulating layers of undoped diamond between BDD elements, these circuits can also be vertically stacked by depositing insulating undoped diamond between them, enabling highly compact and integrated device designs. This enables the development of compact and resilient quantum sensors that combine NV centers with BDD circuitry, presenting a promising avenue for quantum sensing in challenging environments such as industrial sites, deep-sea exploration, and outer space [55].

We also examined whether the BDD omega loop affects the spin properties of the NV ensemble. Spin relaxation and coherence measurements were performed at representative positions in the sensing region, and the results are shown in the Supplementary Information. No clear reduction in T_1, T_2, or T_2^* was observed in the measured region. Regarding crystallographic stress, quantitative stress mapping was not performed in this study. Because the BDD structure is a homoepitaxial layer on diamond, the strain induced by BDD growth is expected to originate mainly from the epitaxial strain near the BDD/NV-diamond interface. Although local changes near the interface cannot be completely excluded, the present measurements indicate that the BDD structure does not cause a clear degradation of the NV spin properties in the region used for the present measurements.

Although a direct comparison of heating effects with Au/Cu metals is desirable, ensuring identical delivered power is non-trivial due to the impedance mismatch; thus, the microwave power generated by a signal generator is not a reliable proxy for the power actually delivered to the device. Therefore, to benchmark the performance practically, we evaluated the frequency shift as a proxy for heating under both short microwave pulses and long continuous microwave drives.

SUPPLEMENTARY MATERIAL

See the Supplementary Material for details of the experimental setup, the BDD fabrication process, electrical resistivity and impedance measurements, AWG-amplitude and microwave-power calibration, estimation procedures for the CW ODMR and Rabi contrasts, spatial Rabi-frequency mapping, Rabi-chevron simulations under heating, Ramsey-based analysis of microwave-induced frequency shifts, and spin relaxation and coherence measurements.

ACKNOWLEDGMENTS

The authors would like to thank H. Sano for helping with impedance measurements. The authors also would like to thank Kenji Ohta for helping with diamond anvil cell preparation. This work is supported by, or in part by, JSPS KAKENHI Grant numbers JP21K14524 and JP23K26528, JSPS Fostering Joint International Research Grant number JP23KK0267, JSPS Bilateral Program Grant number JPJSBP120238803, JST K Program Grant number JPMJKP24F3, the National Research Foundation (NRF) of Korea program under Grant Nos. RS-2024-00442710 and RS-202525454922, Institute of Information & Communications Technology Planning & Evaluation (RS-2025-02219034 and RS-202525464252) and the KIST institutional program (Project No. 26E0011). M.O. receives funding from JSPS Grant-in-Aid for JSPS Fellows Grant number JP24KJ1035. E.K. receives funding from JST SPRING, Japan Grant Number JPMJSP2180.

CONFLICT OF INTEREST

R.M., S.O., Y.T., and K.A. have a patent application pending related to this work.

DATA AVAILABILITY

The data that support the findings of this article are openly available [56].

[1] E. A. Ekimov, V. A. Sidorov, E. D. Bauer, N. N. Mel'nik, N. J. Curro, J. D. Thompson, and S. M. Stishov, Superconductivity in diamond, Nature **428**, 542 (2004).

[2] Y. Takano, M. Nagao, I. Sakaguchi, M. Tachiki, T. Hatano, K. Kobayashi, H. Umezawa, and H. Kawarada, Superconductivity in diamond thin films well above liquid helium temperature, Applied Physics Letters **85**, 2851 (2004).

[3] T. Yokoya, T. Nakamura, T. Matsushita, T. Muro, Y. Takano, M. Nagao, T. Takenouchi, H. Kawarada, and T. Oguchi, Origin of the metallic properties of heavily boron-doped superconducting diamond, Nature **438**, 647 (2005).

[4] Y. Takano, Superconductivity in CVD diamond films, Journal of Physics: Condensed Matter **21**, 253201 (2009).

[5] S. Mandal, T. Bautze, O. A. Williams, C. Naud, É. Bustarret, F. Omnès, P. Rodière, T. Meunier, C. Bäuerle, and L. Saminadayar, The Diamond Superconducting Quantum Interference Device, ACS Nano **5**, 7144 (2011).

[6] T. Kageura, M. Hideko, I. Tsuyuzaki, A. Morishita, A. Kawano, Y. Sasama, T. Yamaguchi, Y. Takano, M. Tachiki, S. Ooi, K. Hirata, S. Arisawa, and H. Kawarada, Single-crystalline boron-doped diamond superconducting quantum interference devices with regrowth-induced step edge structure, Scientific Reports **9**, 15214 (2019).

[7] B. Oripov, D. Kumar, C. Garcia, P. Hemmer, T. Venkatesan, M. S. Ramachandra Rao, and S. M. Anlage, Large microwave inductance of granular boron-doped diamond superconducting films, Applied Physics Letters **118**, 242601 (2021).

[8] J. A. Cuenca, T. Brien, S. Mandal, S. Manifold, S. Doyle, A. Porch, G. M. Klemencic, and O. A. Williams, Superconducting boron doped nanocrystalline diamond microwave coplanar resonator, Carbon **201**, 251 (2023).

[9] J. Isberg, J. Hammersberg, E. Johansson, T. Wikström, D. J. Twitchen, A. J. Whitehead, S. E. Coe, and G. A. Scarsbrook, High Carrier Mobility in Single-Crystal Plasma-Deposited Diamond, Science **297**, 1670 (2002).

[10] M. W. Geis, T. C. Wade, C. H. Wuorio, T. H. Fedynyshyn, B. Duncan, M. E. Plaut, J. O. Varghese, S. M. Warnock, S. A. Vitale, and M. A. Hollis, Progress Toward Diamond Power Field-Effect Transistors, physica status solidi (a) **215**, 1800681 (2018).

[11] N. Donato, N. Rouger, J. Pernot, G. Longobardi, and F. Udrea, Diamond power devices: State of the art, modelling, figures of merit and future perspective, Journal of Physics D: Applied Physics **53**, 093001 (2019).

[12] D. Das, R. Raj, J. Jana, S. Chatterjee, K. L. Ganapathi, M. Chandran, and M. S. R. Rao, Diamond—the ultimate material for exploring physics of spin-defects for quantum technologies and diamondtronics, Journal of Physics D: Applied Physics **55**, 333002 (2022).

[13] F. Jelezko, T. Gaebel, I. Popa, A. Gruber, and J. Wrachtrup, Observation of Coherent Oscillations in a Single Electron Spin, Physical Review Letters **92**, 076401 (2004).

[14] T. Gaebel, M. Domhan, I. Popa, C. Wittmann, P. Neumann, F. Jelezko, J. R. Rabeau, N. Stavrias, A. D. Greentree, S. Prawer, J. Meijer, J. Twamley, P. R. Hemmer, and J. Wrachtrup, Room-temperature coherent coupling of single spins in diamond, Nature Physics **2**, 408 (2006).

[15] F. Jelezko, T. Gaebel, I. Popa, M. Domhan, A. Gruber, and J. Wrachtrup, Observation of Coherent Oscillation of a Single Nuclear Spin and Realization of a Two-Qubit Conditional Quantum Gate, Physical Review Letters **93**, 130501 (2004).

[16] R. Hanson, F. M. Mendoza, R. J. Epstein, and D. D. Awschalom, Polarization and Readout of Coupled Single Spins in Diamond, Physical Review Letters **97**, 087601 (2006).

[17] M. V. G. Dutt, L. Childress, L. Jiang, E. Togan, J. Maze, F. Jelezko, A. S. Zibrov, P. R. Hemmer, and M. D. Lukin, Quantum Register Based on Individual Electronic and Nuclear Spin Qubits in Diamond, Science **316**, 1312 (2007).

[18] J. M. Taylor, P. Cappellaro, L. Childress, L. Jiang, D. Budker, P. R. Hemmer, A. Yacoby, R. Walsworth, and M. D. Lukin, High-sensitivity diamond magnetometer with nanoscale resolution, Nature Physics **4**, 810 (2008).

[19] C. L. Degen, Scanning magnetic field microscope with a diamond single-spin sensor, Applied Physics Letters **92**, 243111 (2008).

[20] G. Balasubramanian, I. Y. Chan, R. Kolesov, M. Al-Hmoud, J. Tisler, C. Shin, C. Kim, A. Wojcik, P. R. Hemmer, A. Krueger, T. Hanke, A. Leitenstorfer, R. Bratschitsch, F. Jelezko, and J. Wrachtrup, Nanoscale imaging magnetometry with diamond spins under ambient conditions, Nature **455**, 648 (2008).

[21] J. R. Maze, P. L. Stanwix, J. S. Hodges, S. Hong, J. M. Taylor, P. Cappellaro, L. Jiang, M. V. G. Dutt, E. Togan, A. S. Zibrov, A. Yacoby, R. L. Walsworth, and M. D. Lukin, Nanoscale magnetic sensing with an individual electronic spin in diamond, Nature **455**, 644 (2008).

[22] V. M. Acosta, E. Bauch, M. P. Ledbetter, C. Santori, K.-M. C. Fu, P. E. Barclay, R. G. Beausoleil, H. Linget, J. F. Roch, F. Treussart, S. Chemerisov, W. Gawlik, and D. Budker, Diamonds with a high density of nitrogen-vacancy centers for magnetometry applications, Physical Review B **80**, 115202 (2009).

[23] E. Schaefer-Nolte, F. Reinhard, M. Ternes, J. Wrachtrup, and K. Kern, A diamond-based scanning probe spin sensor operating at low temperature in ultra-high vacuum, Review of Scientific Instruments **85**, 013701 (2014).

[24] P. Bhattacharyya, W. Chen, X. Huang, S. Chatterjee, B. Huang, B. Kobrin, Y. Lyu, T. J. Smart, M. Block, E. Wang, Z. Wang, W. Wu, S. Hsieh, H. Ma, S. Mandyam, B. Chen, E. Davis, Z. M. Geballe, C. Zu, V. Struzhkin, R. Jeanloz, J. E. Moore, T. Cui, G. Galli, B. I. Halperin, C. R. Laumann, and N. Y. Yao, Imaging the Meissner effect in hydride superconductors using quantum sensors, Nature **627**, 73 (2024).

[25] M. Wang, Y. Wang, Z. Liu, G. Xu, B. Yang, P. Yu, H. Sun, X. Ye, J. Zhou, A. F. Goncharov, Y. Wang, and J. Du, Imaging magnetic transition of magnetite to megabar pressures using quantum sensors in diamond anvil cell, Nature Communications **15**, 8843 (2024).

[26] P. J. Scheidegger, S. Diesch, M. L. Palm, and C. L. Degen, Scanning nitrogen-vacancy magnetometry down to 350 mK, Applied Physics Letters **120**, 224001 (2022).

[27] G.-Q. Liu, X. Feng, N. Wang, Q. Li, and R.-B. Liu, Coherent quantum control of nitrogen-vacancy center spins near 1000 kelvin, Nature Communications **10**, 1344 (2019).

[28] K. Kubota, Y. Hatano, Y. Kainuma, J. Shin, D. Nishitani, C. Shinei, T. Taniguchi, T. Teraji, S. Onoda, T. Ohshima, T. Iwasaki, and M. Hatano, Wide temperature operation of diamond quantum sensor for electric vehicle battery monitoring, Diamond and Related Mate-

rials **135**, 109853 (2023).

[29] J.-W. Fan, S.-W. Guo, C. Lin, N. Wang, G.-Q. Liu, Q. Li, and R.-B. Liu, Quantum Coherence Control at Temperatures up to 1400 K, Nano Letters **24**, 14806 (2024).

[30] M. Lesik, T. Plisson, L. Toraille, J. Renaud, F. Occelli, M. Schmidt, O. Salord, A. Delobbe, T. Debuisschert, L. Rondin, P. Loubeyre, and J.-F. Roch, Magnetic measurements on micrometer-sized samples under high pressure using designed NV centers, Science **366**, 1359 (2019).

[31] K. Y. Yip, K. O. Ho, K. Y. Yu, Y. Chen, W. Zhang, S. Kasahara, Y. Mizukami, T. Shibauchi, Y. Matsuda, S. K. Goh, and S. Yang, Measuring magnetic field texture in correlated electron systems under extreme conditions, Science **366**, 1355 (2019).

[32] S. Hsieh, P. Bhattacharyya, C. Zu, T. Mittiga, T. J. Smart, F. Machado, B. Kobrin, T. O. Höhn, N. Z. Rui, M. Kamrani, S. Chatterjee, S. Choi, M. Zaletel, V. V. Struzhkin, J. E. Moore, V. I. Levitas, R. Jeanloz, and N. Y. Yao, Imaging stress and magnetism at high pressures using a nanoscale quantum sensor, Science **366**, 1349 (2019).

[33] C. Dailledouze, A. Hilberer, M. Schmidt, M.-P. Adam, L. Toraille, K. O. Ho, A. Forget, D. Colson, P. Loubeyre, and J.-F. Roch, Imaging the Meissner effect and flux trapping of superconductors under high pressure using N-V centers, Physical Review Applied **23**, 064067 (2025).

[34] M. W. Doherty, N. B. Manson, P. Delaney, F. Jelezko, J. Wrachtrup, and L. C. L. Hollenberg, The nitrogen-vacancy colour centre in diamond, Physics Reports The Nitrogen-Vacancy Colour Centre in Diamond, **528**, 1 (2013).

[35] L. Jiang, J. S. Hodges, J. R. Maze, P. Maurer, J. M. Taylor, D. G. Cory, P. R. Hemmer, R. L. Walsworth, A. Yacoby, A. S. Zibrov, and M. D. Lukin, Repetitive Readout of a Single Electronic Spin via Quantum Logic with Nuclear Spin Ancillae, Science **326**, 267 (2009).

[36] P. Neumann, J. Beck, M. Steiner, F. Rempp, H. Fedder, P. R. Hemmer, J. Wrachtrup, and F. Jelezko, Single-Shot Readout of a Single Nuclear Spin, Science **329**, 542 (2010).

[37] I. Lovchinsky, A. O. Sushkov, E. Urbach, N. P. de Leon, S. Choi, K. De Greve, R. Evans, R. Gertner, E. Bersin, C. Müller, L. McGuinness, F. Jelezko, R. L. Walsworth, H. Park, and M. D. Lukin, Nuclear magnetic resonance detection and spectroscopy of single proteins using quantum logic, Science **351**, 836 (2016).

[38] K. Arai, C. Belthangady, H. Zhang, N. Bar-Gill, S. J. DeVience, P. Cappellaro, A. Yacoby, and R. L. Walsworth, Fourier magnetic imaging with nanoscale resolution and compressed sensing speed-up using electronic spins in diamond, Nature Nanotechnology **10**, 859 (2015).

[39] H. Zhang, K. Arai, C. Belthangady, J.-C. Jaskula, and R. L. Walsworth, Selective addressing of solid-state spins at the nanoscale via magnetic resonance frequency encoding, npj Quantum Information **3**, 31 (2017).

[40] R. Matsumoto, Y. Sasama, M. Fujioka, T. Irifune, M. Tanaka, T. Yamaguchi, H. Takeya, and Y. Takano, Note: Novel diamond anvil cell for electrical measurements using boron-doped metallic diamond electrodes, Review of Scientific Instruments **87**, 076103 (2016).

[41] E. van Oort, N. B. Manson, and M. Glasbeek, Optically detected spin coherence of the diamond N-V centre in its triplet ground state, Journal of Physics C: Solid State Physics **21**, 4385 (1988).

[42] A. Gruber, A. Dräbenstedt, C. Tietz, L. Fleury, J. Wrachtrup, and C. von Borczyskowski, Scanning Confocal Optical Microscopy and Magnetic Resonance on Single Defect Centers, Science **276**, 2012 (1997).

[43] V. M. Acosta, E. Bauch, M. P. Ledbetter, A. Waxman, L.-S. Bouchard, and D. Budker, Temperature Dependence of the Nitrogen-Vacancy Magnetic Resonance in Diamond, Physical Review Letters **104**, 070801 (2010).

[44] Z. Wang, J. Zhang, X. Feng, and L. Xing, Microwave Heating Effect on Diamond Samples of Nitrogen-Vacancy Centers, ACS Omega **7**, 31538 (2022).

[45] S. Felton, A. M. Edmonds, M. E. Newton, P. M. Martineau, D. Fisher, D. J. Twitchen, and J. M. Baker, Hyperfine interaction in the ground state of the negatively charged nitrogen vacancy center in diamond, Physical Review B **79**, 075203 (2009).

[46] M. W. Doherty, V. V. Struzhkin, D. A. Simpson, L. P. McGuinness, Y. Meng, A. Stacey, T. J. Karle, R. J. Hemley, N. B. Manson, L. C. L. Hollenberg, and S. Prawer, Electronic Properties and Metrology Applications of the Diamond ${\mathrm{NV}}^{\ensuremath{-}}$ Center under Pressure, Physical Review Letters **112**, 047601 (2014).

[47] M. Sasaki, M. Ohkuma, R. Matsumoto, T. Shinmei, T. Irifune, Y. Takano, and K. Shimizu, Enhancement of superconductivity in thin films of Sn under high pressure, Phys. Rev. B **111**, 104513 (2025).

[48] A. Kawano, H. Ishiwata, S. Iriyama, R. Okada, T. Yamaguchi, Y. Takano, and H. Kawarada, Superconductor-to-insulator transition in boron-doped diamond films grown using chemical vapor deposition, Physical Review B **82**, 085318 (2010).

[49] G. D. Fuchs, V. V. Dobrovitski, D. M. Toyli, F. J. Heremans, and D. D. Awschalom, Gigahertz Dynamics of a Strongly Driven Single Quantum Spin, Science **326**, 1520 (2009).

[50] K. Bayat, J. Choy, M. Farrokh Baroughi, S. Meesala, and M. Loncar, Efficient, Uniform, and Large Area Microwave Magnetic Coupling to NV Centers in Diamond Using Double Split-Ring Resonators, Nano Letters **14**, 1208 (2014).

[51] T. Yano, D. A. Tryk, K. Hashimoto, and A. Fujishima, Electrochemical Behavior of Highly Conductive Boron-Doped Diamond Electrodes for Oxygen Reduction in Alkaline Solution, Journal of The Electrochemical Society **145**, 1870 (1998).

[52] D. Gandini, E. Mahé, P. Michaud, W. Haenni, A. Perret, and Ch. Comninellis, Oxidation of carboxylic acids at boron-doped diamond electrodes for wastewater treatment, Journal of Applied Electrochemistry **30**, 1345 (2000).

[53] R. Matsumoto, M. Einaga, S. Adachi, S. Yamamoto, T. Irifune, K. Terashima, H. Takeya, Y. Nakamoto, K. Shimizu, and Y. Takano, Electrical transport measurements for superconducting sulfur hydrides using boron-doped diamond electrodes on beveled diamond anvil, Superconductor Science and Technology **33**, 124005 (2020).

[54] R. Matsumoto, K. Yamane, T. Tadano, K. Terashima, T. Shinmei, T. Irifune, and Y. Takano, Emergence of superconductivity at 20 k in Th_3P_4-type $In_{3-x}S_4$ synthesized by diamond anvil cell with boron-doped diamond electrodes, Chem. Mater. **37**, 1648 (2025).

[55] K.-M. C. Fu, G. Z. Iwata, A. Wickenbrock, and D. Budker, Sensitive magnetometry in challenging environments, AVS Quantum Science **2**, 044702 (2020).

[56] M. Ohkuma, E. Kimura, E. Lee, R. Matsumoto, S. Ohyama, S. Tsuchiya, H. Lim, Y. S. Lee, Y. Takano, J. Lee, and K. Arai, Replication Data for: Coherent control of solid-state defect spins via patterned boron-doped diamond circuit, Zenodo 10.5281/zenodo.14868600 (2025).